PAPER

Check for updates

Mechanistic insight into the non-hydrolytic sol–gel process of tellurite glass films to attain a high transmission†

Xuanzhao Pan,[aef] Jiangbo Zhao, ID *[abe] Gujie Qian,[cd] Xiaozhou Zhang,[aef] Yinlan Ruan,[ae] Andrew Abell ID [aef] and Heike Ebendorff-Heidepriem[ae]

The development of amorphous films with a wide transmission window and high refractive index is of growing significance due to the strong demand of integrating functional nanoparticles for the next-generation hybrid optoelectronic films. High-index TeO_2-based glass films made *via* the sol–gel process are particularly suitable as their low temperature preparation process promises high compatibility with a large variety of nanoparticles and substrates that suffer from low thermal stability. However, due to the lack of in-depth understanding of the mechanisms of the formation of undesired metallic-Te (highly absorbing species) in the films, the preparation of high-transmission TeO_2-based sol–gel films has been severely hampered. Here, by gaining insight into the mechanistic chemistry of metallic-Te formation at different stages during the non-hydrolytic sol–gel process, we identify the chemical route to prevent the generation of metallic-Te in a TeO_2-based film. The as-prepared TeO_2-based film exhibits a high transmission that is close to the theoretical limit. This opens up a new avenue for advancing the performance of hybrid optoelectronic films *via* incorporating a large variety of unique nanoparticles.

1. Introduction

Over the past decades, advanced hybrid optoelectronic films have been widely studied and developed for a broad range of applications that rely on integrating various functional nanoparticles into an amorphous matrix.[1–15] Since the majority of optoelectronic nanoparticles have high refractive indices, *e.g.*, ITO nanoparticles (index = 1.54 (ref. 16)), nanodiamond (index = 2.4 (ref. 17)), nanoruby (index = 1.76 (ref. 18)), and quantum dots (index > 2.0 (ref. 19)), extensive efforts have been made to develop (visible) transparent films with high refractive indices. Besides attaining the transparency of the film itself, the reduced index contrast between the incorporated nanoparticles and the films can significantly suppress the scattering, which in turn retains the transparency of the hybrid films but also enhances the efficiency for light delivery and optical signal collection.[20]

[a]*Institute for Photonics and Advanced Sensing, University of Adelaide, Adelaide, SA 5005, Australia. E-mail: tim.zhao@adelaide.edu.au*

[b]*Leibniz Institute of Photonic Technology, Jena 07745, Germany*

[c]*Natural and Built Environments Research Centre, School of Natural and Built Environments, University of South Australia, Mawson Lakes, SA 5095, Australia*

[d]*College of Science and Engineering, Flinders University, Bedford Park, SA 5042, Australia*

[e]*Centre for Nanoscale BioPhotonics, University of Adelaide, Adelaide, SA, Australia*

[f]*Department of Chemistry, School of Physical Sciences, The University of Adelaide, South Australia, Australia*

† Electronic supplementary information (ESI) available. See DOI: 10.1039/c9ra10731b

Due to the simplicity, cost-effectiveness, compositional flexibility, and compatibility with different nanoparticles,[13,14,21] the sol–gel method has been used to prepare inorganic high-index films that can exhibit a wide transmission window with superior chemical resistance and thermal stability, such as Al_2O_3 (transmission 0.2–6 μm, index = 1.68),[22] TiO_2 (transmission 0.45–5 μm, index = 2.41)[23] and ZrO_2 (transmission 0.38–7 μm, index = 2.16).[24] However, preparing those films with high quality requires the processing at a relatively high temperature, *e.g.*, >450 °C,[25,26] >500 °C,[6,9] and >600 °C,[27] respectively. This limits the incorporation of NPs and/or use of substrates that have superior or unique optoelectronic properties but are subject to low thermal stability. TeO_2-based sol–gel films present an attractive alternative, since they not only exhibit high refractive index (n_D = 1.999–2.2743, dependent on glass composition)[20,28] as well as high transmission over a wide spectral range (0.33–5 μm), but more importantly, can be prepared using a much lower sol–gel processing temperature (*e.g.*, ~300 °C) compared to conventional Al_2O_3, TiO_2 and ZrO_2 based films. This suggests TeO_2 films can be a promising candidate for the development of hybrid optoelectronic films.[29,30]

The preparation of TeO_2-based films using the conventional hydrolytic sol–gel (HSG) chemistry suffers from the Te-alkoxide precursor readily undergoing detrimental hydrolysis instead of the desired polymerization.[31,32] To circumvent this obstacle, a non-hydrolytic sol–gel (NHSG) chemical route was developed,[29,30] with Na_2O and ZnO introduced as network modifier[30]

Paper

RSC Advances

and network intermediate,[29,33] respectively. Yet hitherto, the NHSG route has not been developed to a procedure that completely prevents the formation of metallic-Te and/or oxide crystals during the preparation of TeO$_2$-based sol–gel glass films. This has hampered the tellurite sol–gel glass films achieving their theoretical limit in optical transmission spanning from the UV to infrared wavelength range.[34–38] The unmet challenge of attaining metallic-Te and crystal free TeO$_2$-based sol–gel films is largely ascribed to the lack of in-depth and comprehensive understanding of how these undesired species are formed.

Here, we elucidated the mechanisms of forming metallic-Te during the preparation of TeO$_2$-based glass films *via* the NHSG route, *e.g.*, 80TeO$_2$–10ZnO–10Na$_2$O (TZN) in this work. Using a series of structural analysis of the products from different sol–gel steps, we revealed that, in the process of removing organic groups (OGs) under heat to produce a dense glass, the fractions of OGs in the xerogels (intermediate product in the sol–gel process) determine the formation of metallic-Te. Based upon the insight into the kinetics and thermodynamics of the polymerization reactions, we fine-tuned the processing conditions to suppress the fractions of OGs during xerogel preparation, which enabled to prevent the formation of metallic-Te in the TZN glass films. This in-depth understanding into the chemistry of producing TZN glass film *via* the NHSG route has allowed us to produce a high-transmission TZN glass film, which shows, to the best of our knowledge, the transmission closest to the theoretical limit over the visible spectral range.

2. Experimental

2.1. TZN glass film preparation

The NHSG-based TZN glass films were prepared *via* a five-step procedure (Fig. 1, and experimental details in ESI and Fig. S1†), comprising molecular Te-alkoxide preparation, TZN sol preparation, sol aging to enhance polymerization, sol heating to obtain dry porous xerogel, and finally xerogel heating to form inorganic glass film.

The first step is the preparation of high purity Te-alkoxide (Te(O$_2$C$_3$H$_6$)$_2$) *via* an alcoholization reaction between TeO$_2$ powder and 1,2-propanediol solvent,[39–41] catalyzed with *p*-toluene sulfonic acid (PTSA). This reaction takes place when anhydrous α-TeO$_2$ and PTSA monohydrate are dispersed and dissolved in 1,2-propanediol at 150 °C (with reflux). Details of the chemical reactions are described in Section 3.2.

The second step is to prepare the TZN sol, which is the precursor for the subsequent NHSG process. TZN sol is formed by heating the mixture of Te-alkoxide molecules, Na-acetate and Zn-acetate in 1,2 propanediol at 80 °C (with reflux), followed by a high-speed centrifugation (14 800 rpm for 15 min) to remove any impurities. Te-alkoxide, Zn-acetate and Na-acetate are added in molar ratio of Te : Zn : Na = 80 : 10 : 20.

In the third step, aging the sol at room temperature over weeks or months in a closed glass vial is conducted to prepare the so-called aged TZN sol. This relates to the fact that the polymerization of the TZN sol occurs at room temperature to a different extent, dependent on the aging duration (details described in Section 3.3). The sol-aging times of 9 days (F), 60 days (S), 90 days (M) and 300 days (L) were applied, where F, S, M and L denote fresh-aged, short-aged, medium-aged and long-aged sol, respectively.

In the fourth step, heating aged sol at temperatures between 80–150 °C for 12–72 h obtains the dry porous xerogel *via* simultaneously evaporating the solvent and facilitating the polymerization. Two different forms of xerogel samples, dry xerogel powders and dry xerogel films, were prepared in this work.

In the final step, the compact, pore-free, inorganic TZN glass films with the nominal molar composition of 80TeO$_2$–10ZnO–10Na$_2$O are acquired by heating the xerogel films at the temperatures of ≥300 °C for 1 h. The temperature was reached using a rate of 1 °C min^{-1} from room temperature.

Table 1 lists the xerogel powders used for thermal analysis and the xerogel/glass film samples used for optical transmission measurements, X-ray diffraction (XRD) and scanning confocal microscope (SCM) analysis. Transparent glass coverslips were used as film substrates for the optical transmission measurements, while Si wafers were used as substrates for XRD and SCM measurements.

2.2. Sample characterizations

The transmission spectra of the TZN-based films on glass coverslips and an uncoated glass coverslip over the wavelength from 300 to 800 nm were acquired using a UV-Vis spectrophotometer (Cary 5000, Agilent Technologies).
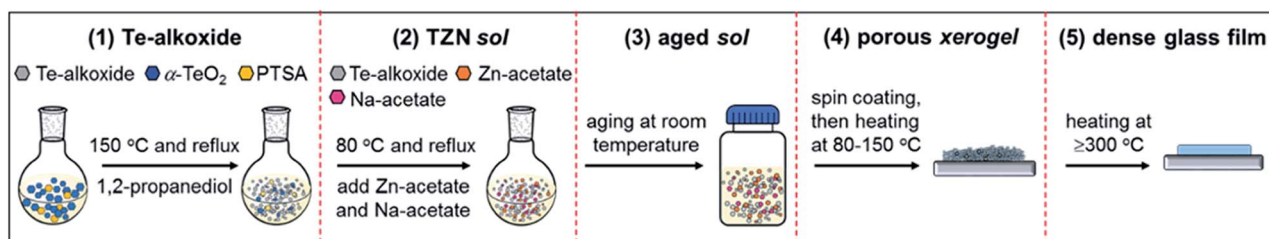

Fig. 1 Schematic illustration of the five-step procedure to prepare dense TZN glass films. (1) Te-alkoxide synthesized *via* a catalytic cycle reaction at 150 °C under reflux with starting materials of TeO$_2$, *p*-toluene sulfonic acid monohydrate crystals (PTSA) and 1,2-propanediol. (2) TZN sol prepared *via* mixing Te-alkoxide, Na-acetate and Zn-acetate in 1,2-propanediol at 80 °C under reflux. (3) Aged sol prepared *via* storing the sol at room temperature in a sealed flask for 9–300 days. (4) Porous xerogel film made by heating the wet sol film (made *via* spin coating) at 80–150 °C for 12–72 h. (5) Dense glass film prepared by heating the porous xerogel films at ≥300 °C.

Table 1 Summary of the xerogel powders and xerogel/glass film samples prepared *via* various conditions, including sol-aging time, sol-heating temperature, and xerogel heating temperature. The sol-aging time is classified into 4 categories: "fresh (F)" 9 days, "short (S)" 30–60 days, "medium (M)" 90 days and "long (L)" 300 days

Samples	Sample code	Sol aging (days)	Sol heating (°C-days)	Xerogel heating (°C)
Xerogel powder	F-80	9	80-3	
	F-150	9	150-1	
	S-130	60	130-1	
	M-80	90	80-3	
	L-80	300	80-3	
Xerogel/glass film	S-130	30	130-0.5	
	S-130-200	30	130-0.5 and 200-0.5	
	S-130-300	30	130-0.5	300
	S-130-400	30	130-0.5	400
	S-130-500	30	130-0.5	500
	S-80-300	60	80-0.5	300
	S-150-300	60	80-0.5	300

Micro-XRD of the TZN-based films on Si wafers was measured using a micro-diffractometer (D/MAX-Rapid II Microdiffractometer, Rigaku) with a Cobalt K_α radiation (wavelength 1.7902 Å, accelerating voltage 40 kV, and filament current 15 mA) at a fixed incident angle of 10 degree. The computer software 2DP was used to convert original 2D imaging data (Debye–Scherrer rings) collected from the curved imaging plate to 1D profiles (*i.e.* intensity *vs.* 2θ), during which, the diffraction signal of Si is eliminated. Powder-XRD of the TZN-based powders was measured using a diffractometer (Rigaku Miniflex600) with a copper K_α radiation (wavelength 1.5418 Å, accelerating voltage 40 kV, filament current 15 mA, and scanning speed $3°min^{-1}$). The crystalline phases of both micro-XRD and powder-XRD analysis were indexed using the ICDD PDF-2 database.

Thermogravimetric and differential scanning calorimetry (TG-DSC) analysis of TZN xerogel powders were performed over the range of 30 to 700 °C by a thermal analysis system (TG-DSC 2 STARe, Mettler Toledo). In order to visualize the rate of weight change across the temperature range under consideration, the first derivative of TG data was calculated for differentiate-TG analysis (DTG). The TG-DSC curves of all powder samples in an alumina crucible were acquired with a ramping rate of $10 °C min^{-1}$ under specific atmosphere, *i.e.* 20% O_2 + 80% N_2 and 80% O_2 + 20% N_2 with flow rate of 3 L min^{-1}, respectively.

The gaseous molecules discharged from heating TZN xerogels (30–350 °C) were monitored by simultaneous thermal analysis (STA) hyphenated Fourier transform infrared spectroscopy (vapor-FTIR) (Spectrum 400, PerkinElmer). The vibrational spectra of the gaseous molecules were recorded in the wavenumber range of 500–4000 cm^{-1}, with a resolution of 2 cm^{-1}. The sample chamber was heated at a ramp rate of $5 °C min^{-1}$ and purged with dry air (1.8 L min^{-1}).

Confocal scanning microscope images and fluorescence spectra of TZN-based films were collected by an in-house built scanning confocal microscope. The collimated laser beam 532 nm with a power of 2.56 μW was focused onto and scanned across the film samples over an area of 200 × 200 μm with a stepping resolution of 1 μm per step. The fluorescence signal

was delivered to a photon counts detector (SPCM, Excelitas Technologies) and converted to color images. For the spectra acquisition, a flip mirror was used to direct the fluorescence signal to a spectrometer (iHR320 spectrometer HORIBA Scientific) with an exposure time of 30 s.

3. Results and discussion

3.1. Impact of sol heating and xerogel heating on metallic-Te and tellurite crystal formation

We commenced with using the previously reported processing conditions;[29,30] the S-130-300 TZN glass film was produced *via* spin-coating short-aged sol on a glass coverslip, followed by heating (in air) at 130 °C for 12 h to form a dry xerogel film and then heating at 300 °C for 1 h to obtain a dense glass film. This glass film shows relatively good transmission but a brown color appearance (Fig. 2a). Based upon previous observations for other tellurite-based glass films[42] and bulk tellurite glass,[43] this color appearance is attributed to the presence of reduced tellurium species or metallic-Te.[30,35,42]

In order to eliminate the undesired color *via* oxidization of the metallic-Te in the film, higher xerogel heating temperatures of 400 °C and 500 °C were applied. The increased xerogel heating temperatures successfully eliminated the brown color but led to white and opaque appearance (Fig. 2a). These visual characteristics are reflected in the transmission spectra (Fig. 2c). Relative to the spectrum of an uncoated glass coverslip, the S-130-300 glass film exhibits a lower transmission over the measured wavelength range of 300–800 nm. The low transmission particularly in the UV-blue spectral range is associated with the presence of metallic-Te.[42] The low transmission at 800 nm suggests that the metallic-Te exhibits scattering that extends into the infrared region. In contrast to the S-130-300 glass film, the transmission spectra of the S-130-400 and S-130-500 glass films show higher UV-blue transmission, but lower transmission at longer wavelengths >440 nm, which is consistent with their opaque white appearance.

In agreement with the transmission measurements, micro-XRD analysis indicates the diffraction peaks of metallic-Te for
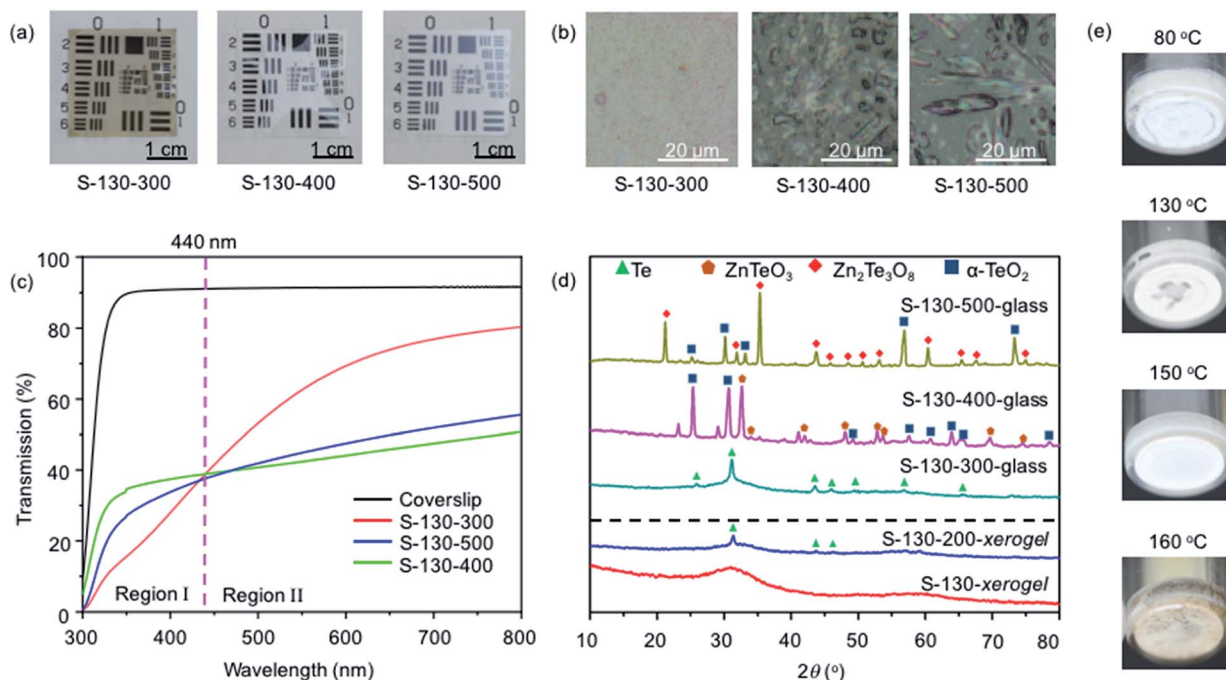
Fig. 2 Characterizations of TZN films and xerogel powders. (a) Photographs, (b) optical microscope images, and (c) transmission spectra of TZN glass films on glass coverslips. (d) Micro-XRD patterns of TZN films on Si wafers, where the narrow diffractions indicate the presence of crystal phases, while the broad 'hump' at ~32° reflects the amorphous characteristic. (e) Photographs of xerogel powders made by heating short-aged sol at 80, 130, 150 and 160 °C.

the S-130-300 film but not for the S130-400 and S-130-500 samples (Fig. 2d). The optical micrographs (Fig. 2b) show that the glass films processed at higher temperatures of 400 °C and 500 °C contain micron-sized crystals with different morphologies (mainly platelets at 400 °C and mainly needles at 500 °C), suggesting the formation of different crystal phases at 400 °C and 500 °C, respectively. This was confirmed by micro-XRD, showing the diffraction peaks of $ZnTeO_3$ crystals for S-130-400 and those of $Zn_2Te_3O_8$ crystals for S-130-500 films. In addition, α-TeO_2 diffractions were found in both films.[30,34] The optical microscopy and XRD results are consistent with the opaque white appearance and overall reduced transmission of the S-130-400 and S-130-500 films.

To determine the temperature threshold of forming metallic-Te, XRD was used to analyze the xerogel films S-130 and S-130-200 (Fig. 2d). It shows that the S-130 film only exhibits a broad diffraction 'hump', corresponding to an amorphous structure, whereas the S-130-200 film gives the characteristic diffraction peaks of metallic-Te. To determine more precisely the onset temperature of generating metallic-Te, xerogel powders were prepared by heating short-aged sol using different temperatures of 80, 130, 150, 160 °C. These xerogel powders show that only the 160 °C-processed powder displays the brown appearance of metallic-Te (Fig. 2e), suggesting formation of metallic-Te commences around 160 °C. This is consistent with the observation in producing S-130-200 film, where heating of the S-130 xerogel film at 200 °C led to the metallic-Te.

The characterization results of the TZN film and powder samples reveal that metallic-Te is formed when heating sol or

xerogel samples at temperatures >150 °C but <350 °C. The amount of metallic-Te is increased for higher xerogel heating temperature of 300 °C compared to 200 °C. Further increase of xerogel heating temperatures to 400 °C and 500 °C induces oxidation of metallic-Te (formed at lower temperatures) into crystalline TeO_2 and other crystallinity in TZN glass.[34] These results suggest the only pathway of obtaining a high-transparency colorless TZN glass film lies in preventing the formation of metallic-Te prior to or during heating the xerogels into a dense glass.

For this purpose, the chemistry with respect to metallic-Te formation at different stages during NHSG synthesis is investigated in detail in the following sections, with the aim to identify suitable synthesis conditions to achieve metallic-Te free TZN glass films.

3.2. Chemical reactions during preparation of Te-alkoxide precursor

As shown in Fig. 3a (black arrows), the catalyzed alcoholization reactions of producing Te-alkoxide molecules begins when the hydrogen atom (H) of the sulfonic acid group of PTSA is displaced by Te in TeO_2 at 150 °C. This forms the intermediate compound p-toluene sulfonic tellurium (PTS-Te),[39–41] followed by the exchange of the H atom of the hydroxyl groups of 1,2-propanediol with the Te atom of the intermediate PTS-Te. The desired Te-alkoxide is obtained and the catalyst PTSA is regenerated to participate in another catalytic cycle.[39] The resultant Te-alkoxide dissolved in the solution (Fig. 3a, bottom-middle photo), was separated from the sediment via hot filtration; the
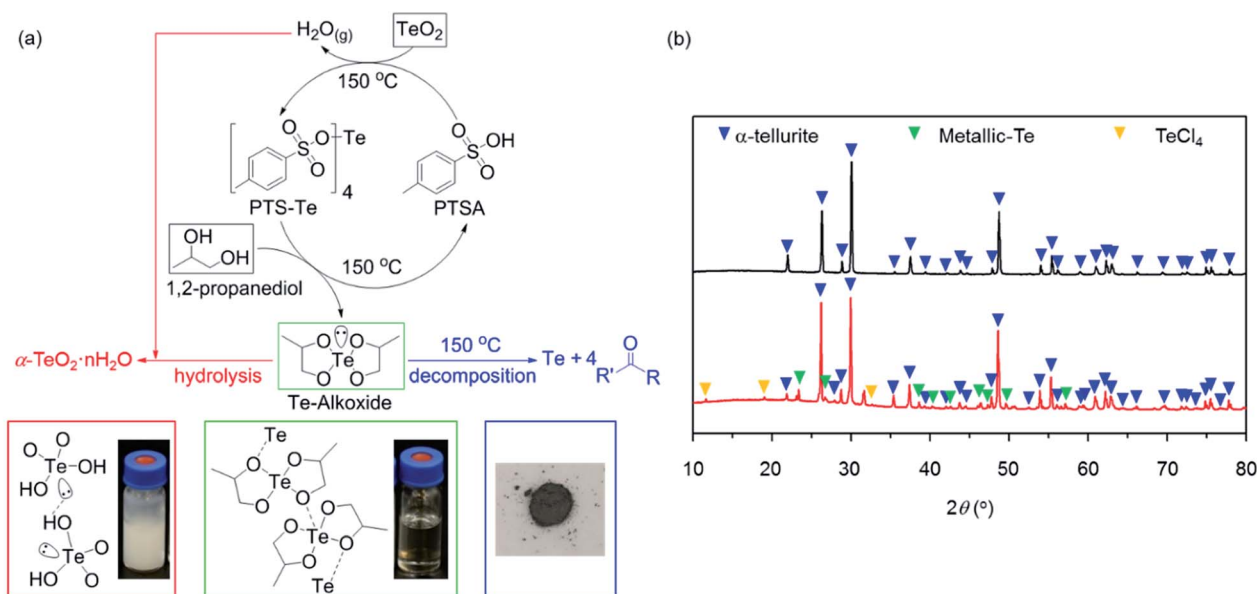
Fig. 3 Chemical reactions during Te-alkoxide preparation. (a) Catalyzed cyclic alcoholization between TeO_2 and 1,2-propanediol generates Te-alkoxide molecules (black arrows). Hydrolysis of Te-alkoxide by *in situ* formed H_2O results in the formation of undesired amorphous TeO_2 hydrolytic gel (red arrows). Under the thermal activation of 150 °C, Te-alkoxide decomposes to metallic-Te and carbonyl compound (R and R′ are organic groups) (blue arrow). The bottom photos from left to right correspond to the TeO_2 hydrolytic gel (formed *via* enhanced hydrolysis by adding H_2O to Te-alkoxide solution), the as-prepared transparent Te-alkoxide solution, and HCl acid-treated sediment. (b) Powder-XRD of the collected sediment before (top graph) and after (bottom graph) HCl treatment.

latter contains white powder with interspersed black particles (Fig. S4†). The generation of Te-alkoxide $Te(O_2C_3H_6)_2$ (green framed in Fig. 3a) with a molecular weight of 278 g mol^{-1} (isotope ^{130}Te) was confirmed by electrospray ionization mass spectrometry measurement.

In the Te-alkoxide molecule, the Te atom is coordinated with the four oxygen atoms of the two branched alkoxy groups, denoted as the intramolecular Te–O bonds. The lone pair of electrons (LPE) of the Te atom leads to a bipyramidal coordination geometry for Te and a weak intermolecular bond between Te-alkoxide molecules, depicted by a dotted line Te⋯O (Fig. 3a, bottom-middle molecular structure).[30]

The white powder and the black particles of the sediment indicate undesired formation of TeO_2 precipitate and metallic-Te, respectively, due to the side reactions of hydrolysis and thermal decomposition, which are facilitated by the LPE and bipyramidal coordination of the Te atom as follows.

During the alcoholization forming Te-alkoxide *via* liberation of H and O from PTSA and TeO_2, H_2O is *in situ* produced. The nucleophilic attack of O in H_2O to the bipyramidal coordinated Te in the Te-alkoxide molecule can occur,[44] corresponding to a process known as hydrolysis (Fig. 3a, red arrows). To illustrate the effect of hydrolysis reaction, a large amount of H_2O (much more than H_2O generated *in situ*) was intentionally added to the Te-alkoxide solution, resulting in a white TeO_2 precipitate (Fig. 3a, bottom-left). This hydrolysis effect agrees with the sediment by-product containing white powder.

As a consequence of the LPE weakening effect, the Te–O bond can be relatively easily broken, particularly under thermal

activation. This bond cleavage leads to decomposition of Te-alkoxide molecules into metallic-Te and carbonyl-containing (C=O) compounds (Fig. 3a, blue arrow). In order to confirm that the black particles in the sediment are metallic-Te, powder-XRD measurement of the collected sediment was used. However, only α-TeO_2 diffractions were detected (Fig. 3b, top graph). Given that TeO_2 is soluble in HCl solution but not metallic-Te, the sediment was processed by HCl to extract metallic-Te from the large amount of TeO_2. As shown in Fig. 3a (bottom-right photo) and Fig. 3b, the diffractions of HCl-treated sediment show the metallic-Te peaks, confirming the source of the black particles in the sediment, which results from the thermal decomposition. In addition, $TeCl_4$ and α-TeO_2 diffractions were observed (Fig. 3b, bottom graph), which are attributed to the reaction between TeO_2 and HCl, and residual TeO_2, respectively.

3.3. Insight into chemical reactions during sol aging, sol heating and xerogel heating

3.3.1. Overview of TG-DSC results. The onset temperature of forming metallic-Te during the preparation of sol and xerogel was determined to be ∼160 °C (Fig. 2e). Transforming OG-containing xerogel into OG-free (inorganic) glass requires heating temperatures ≥300 °C, which is markedly higher than the threshold temperature of metallic-Te formation (∼160 °C). In order to identify how to avoid metallic-Te formation despite using xerogel heating temperature above the onset temperature, we investigated the impact of preparation conditions sol aging, sol heating and xerogel heating on the extent of metallic-Te

formation, by using TG-DSC measurements on a series of TZN xerogel powders. To this end, F/M/L-80 samples were prepared at low sol-heating temperature of 80 °C, using different sol aging time (9, 60, 300 days). F-150 sample was prepared at high sol heating temperature of 150 °C with 9 days sol aging. In addition, S-130 sample was prepared using the same sol heating temperature (130 °C) and sol aging time (60 days) as for the S-130 xerogel film described in Section 3.1 (Fig. 2a).

The TG-DTG-DSC curves of all xerogel powders can be classified into five different regions (I–V) as shown in Fig. 4:

I: 30 to 100 °C: the residual solvent evaporation leads to small TG weight loss of 1–4% for various xerogel powders.

II: 100 to ~250 °C: the liberation of OGs *via* an endothermic reaction results in varying weight loss, corresponding to the DTG peak with an endothermic DSC dip.

III: ~250 to 300 °C: the weight loss relevant to the liberation of OGs *via* an exothermic reaction appears in this region, indicated by the DTG peak in accompany with an exothermic DSC peak. This observation is opposite to the endothermic liberation of OGs in region II.

IV: 300 to ~500 °C: negligible weight loss is observed for all xerogel samples heated at temperatures >300 °C, indicating the

OGs are completely removed. The pronounced narrow endothermic DSC dip at 443–449 °C is ascribed to the melting of metallic-Te in accordance with the melting temperature of bulk tellurium (449 °C).[45] This suggests metallic-Te is formed in S/M-80, S-130 and F-150 samples. The absence of the metallic-Te peak in the F-80 sample is related to the evaporation of Te-alkoxide prior to forming metallic-Te (detailed explanation in the ESI†). The exothermic DSC peaks at ~360, ~400 and ~460 °C are attributed to the formation of TeO_2, $ZnTeO_3$ and $Zn_2Te_3O_8$ crystals as identified in tellurite glass (Fig. S5†)[46–48] and in S-130-400 and S-130-500 glass films (Fig. 2d).

V: >500 °C: further increase of the heating temperature melts the crystals formed in the region IV and the glass film itself, corresponding to the broad endothermic dip with negligible weight loss.

In regions II and III, the different xerogel samples show profound differences of weight losses, as indicated in the caption of Fig. 4. With increasing sol aging time, the ratio of weight loss in region III is enhanced relative to region II, *e.g.*, from 9 to 300 days, the ratio increases from 0.2 to 0.8. The ratio is particularly large with a value of 8 for the sol heated at 150 °C. In addition, with increasing sol aging time, the total weight loss
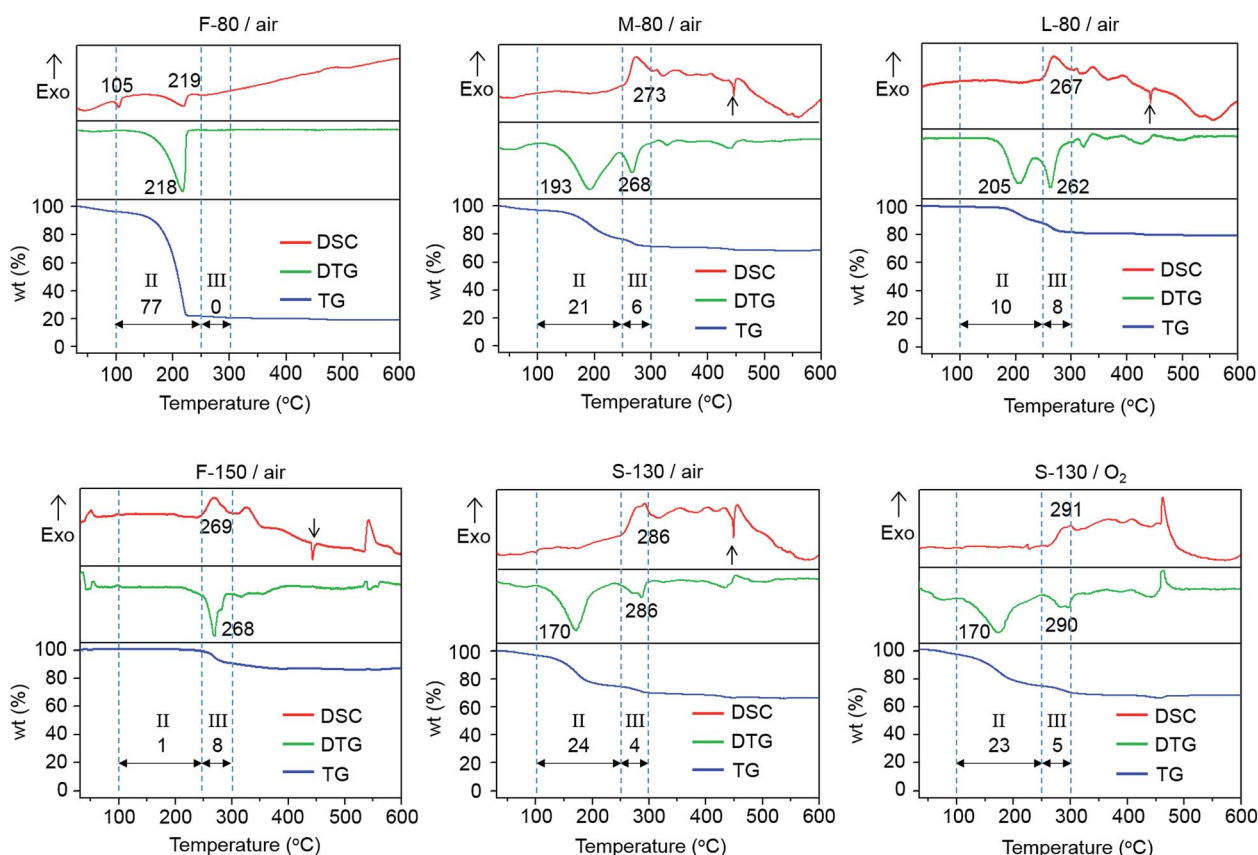

Fig. 4 TG-DTG-DSC analysis of various xerogel powders under gas flow of 20% O_2/80% N_2 (referred to as air in the name panel of each sub-figure), or 80% O_2/20% N_2 (referred to as O_2 in the name panel of the sub-figure). Other preparation conditions (sol aging time and sol heating temperature) for the xerogel samples are given in the name panel above each sub-figure. The temperatures listed in the graphs of the DTG and DSC curves correspond to the DTG and DSC dips/peaks in regions of II and III, respectively. The numbers above the horizontal arrows at the bottom panel of each graph represent wt% of weight loss in regions II and III, respectively, normalized to total weight loss in these two regions. The short black vertical arrows pointing at the endothermic dip of 446–449 °C at the top panel of DSC curves assign to the melting of metallic-Te. The ratios of weight loss in region III over region II are 0.0, 0.3, 0.8, 8.0 and 0.2 for F-80, M-80, L-80, F-150, S-130, respectively.

over 100–300 °C in regions II and III decreases (from 77% for 9 days to 18% for 300 days). Surprisingly, the use of 150 °C sol heating temperature leads to a particularly low weight loss (9%). Given that the weight loss during xerogel heating (in regions II and III) originates from the liberation of OGs, these results suggest that OG liberation is highly dependent on the conditions of preparing xerogel, including sol aging and sol heating.

For the xerogel powder samples (S/M-80, S-130 and F-150) and the xerogel film samples (S-130-200 and S-130-300), both the metallic-Te formation and OG liberation coincide in the same temperature range of 160–300 °C. This strongly implies that the liberated OGs reduce Te(IV) into Te(0), *i.e.*, the formation of metallic-Te.[30] Therefore, the decisive factor in determining the formation of metallic-Te is closely related to the conditions used to prepare the xerogel samples. To elucidate this interrelation, we studied how these conditions affect the polymerization reactions and in which way they govern the amount of OGs in the xerogel.

3.3.2. Polymerization reactions forming the xerogel network. The polymerization process of addition reaction (so-called addition polymerization) has been demonstrated to generate a xerogel network *via* binding the Te-alkoxide precursor molecules.[30] Initially, the Te–O bond weakened by LPE would be subject to heterolytic cleavage of Te–O and C–O bonds (in different Te-alkoxide precursor molecules, as shown in the grey box in Fig. 5). New covalent C–O–C bonds are subsequently formed between these disrupted molecules, and weak intermolecular Te···O–Te bonds are transformed to strong intramolecular Te–O–Te bond. In this process, an O–R–O group with R = CH(CH$_3$)–CH$_2$ (hereafter referred to as cyclic group) is

disrupted and transformed into a short –O– bridge (hereafter referred to as oxo bridge) and a long –O–R–O–R–O– bridge (hereafter referred to as alkoxy bridge).

For our TZN sol composition with molar ratio of 80 Te-alkoxide : 10 Zn-acetate : 20 Na-acetate, the complete removal of all OGs, *i.e.* the liberation of $C_6H_{12}O_4$ from $Te(O_2C_3H_6)_2$, and $C_4H_6O_4$ from $Zn(C_2H_3O_2)_2$ and $(NaC_2H_3O_2)_2$, corresponds to a theoretical weight loss of 44 wt%. Intriguingly, the experimental weight losses in regions II and III for the xerogel samples of M/L-80, S-130 and F-150 are within 9–28 wt% (Fig. 4), all of which are considerably lower than the theoretical weight loss. Since the liberation of OGs is completed at the upper bound temperature of region III (300 °C), the weight loss discrepancy between the experimental observation and theoretical expectation can only result from the liberation of OGs prior to the TG-DSC analysis. In other words, a part the of OGs is already liberated during sol aging and sol heating before xerogel heating.

The liberation of OGs during xerogel preparation suggests that the condensation polymerization, which is accompanied with elimination of OGs, is involved in forming the xerogel network, rather than only the addition polymerization as proposed in ref. 30. This agrees with the fact that the condensation reaction is the leading polymerization mechanism in sol–gel chemistry.[49] As the addition reaction involves C–O and Te–O bond cleavages within cyclic groups of different Te-alkoxide molecules (grey box in Fig. 5), we propose that the condensation reaction occurs concurrently within the same alkoxy bridge *via* C–O and Te–O bond cleavages (light-yellow box in Fig. 5), leading to new oxo bridges between Te atoms through the release of small OGs.
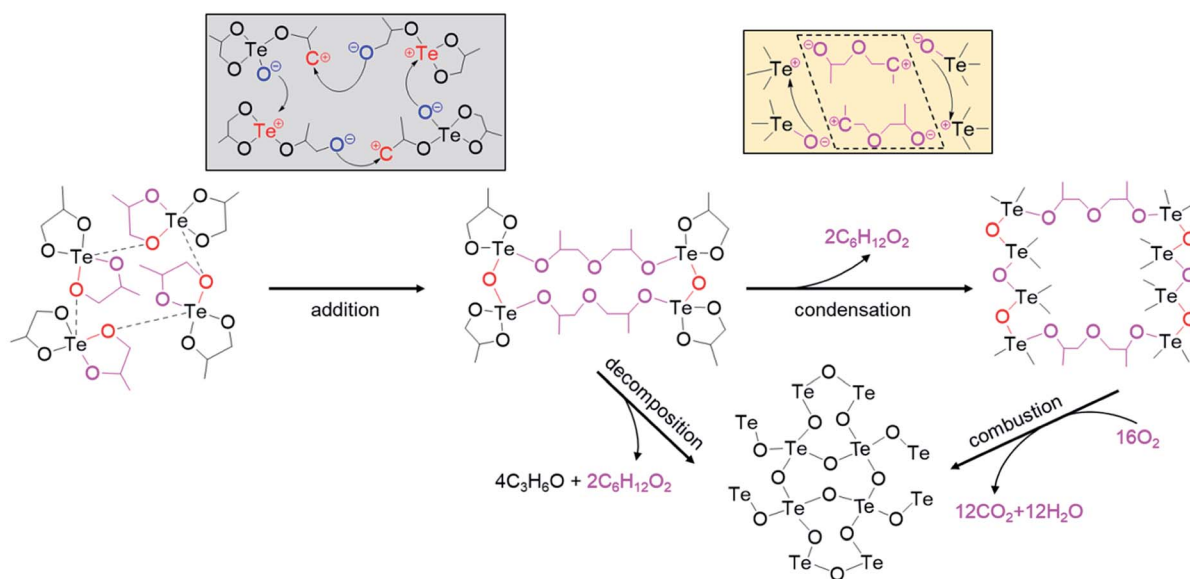

Fig. 5 Schematic illustration of the chemical formulae of the reactions towards forming dense TZN glass. The weakly linked Te-alkoxide molecules are used as a precursor to produce a ring-shaped molecule *via* addition reaction. The ring-shaped molecules undergo either a decomposition reaction, or sequential condensation and combustion reactions to generate an inorganic glass network. The schematics in the shaded boxes show the respective bond forming mechanisms: addition polymerization reaction (grey box) initialized by the Te–O and C–O bond cleavages within Te-alkoxide molecules, and condensation polymerization reaction (light-yellow box) within alkoxy bridges.

Given that the condensation reaction is based on bond cleavages within alkoxy bridges that are formed *via* addition reaction, the condensation reaction can only proceed with the occurrence of the addition reaction. This agrees with the previous report that the condensation reaction in NHSG systems is catalyzed by their own reaction products.[49] Accordingly, we identify that both polymerization reactions contribute to the resultant xerogel network to different extents, depending on the sol aging time and sol heating temperature used to prepare the xerogel.

In conclusion, the evolution of the xerogel network commences with the addition reaction, leading to the formation of alkoxy bridges, which allows the condensation reaction to occur concurrently. Both polymerization processes contribute to the formation of the resultant xerogel network to different extents depending on the sol aging time and sol heating temperature employed to prepare the xerogel. To reveal the impact of the extent of the polymerization reactions on the thermal behavior of a xerogel, we developed the following structural model of $[TeO_4]$ polyhedra in the xerogel network.

3.3.3. Structural model of the xerogel network. Analogous to the structural units of TeO_2 crystals and TeO_2-based glasses, the basic unit of Te-alkoxide is a trigonal bipyramidal $[TeO_4]$ polyhedron with the oxygen atoms at four corners.[50] These bipyramidal $[TeO_4]$ polyhedra can be connected either *via* oxo bridges (*i.e.* two adjacent polyhedra share a corner, as in crystalline and amorphous TeO_2)[50] or *via* alkoxy bridges (*i.e.* two adjacent polyhedra share an alkoxy bridge) in the xerogel network. This flexibility leads to various types of polyhedral $[TeO_4]$ to constitute the xerogel network, as depicted in Fig. 6:

• 'P' polyhedra (precursor molecules): they refer to $[TeO_4]$ polyhedra only consisting of cyclic groups. They are dispersed individually without forming oxo or alkoxy bridges with adjacent polyhedra. 'P' polyhedra are found in a low-degree polymerized xerogel network.

• 'O' polyhedra: these are formed *via* condensation reaction that liberates OGs, leading to the formation of oxo bridges. Therefore, alkoxy bridges are absent in 'O' polyhedra.

• 'A' polyhedra: these are formed *via* addition reaction that forms at least one alkoxy bridge. An 'A' polyhedron exhibits either (1) one cyclic group, one oxo bridge and one alkoxy bridge, or (2) two oxo and two alkoxy bridges. The presence of alkoxy bridges makes 'A' polyhedra the source of liberating OGs upon heating. The bond rearrangements (bond cleavages and bond formation) during OG liberation result in two types of 'A' polyhedra that differ by the presence or absence of alkoxy bridges in their second and third nearest neighborhood, as illustrated in Fig. 6. Specifically,

- 'Aa' polyhedra: they are surrounded by other 'A' polyhedra *via* alkoxy bridges, *i.e.* they are embedded in a network with many alkoxy bridges and cyclic groups.

- 'Ao' polyhedra: they are surrounded by 'O' polyhedra.

The short oxo and long alkoxy bridges exhibit different conformational mobility, which leads to high and low steric hindrance of the polyhedra network, respectively. As the polyhedra differ in their types of bridges (and thus in their conformational mobility), the four types of polyhedra cause different liberation rates of OGs, *i.e.*, different thermal behaviors upon heating (Fig. S6†):

• 'P' polyhedra are essentially precursor molecules and thus are expected to show the same thermal behavior as Te-alkoxide crystals (Fig. S7†), namely melting at ~105 °C and evaporation at higher temperatures ≤250 °C. This leads to large weight loss in region II.

• 'Aa' polyhedra are connected *via* alkoxy-bridges with high conformational mobility. Thus, they liberate their OGs *via* endothermic decomposition, resulting in weight loss in the low temperature range of region II.

• 'Ao' polyhedra are surrounded by polyhedra with low conformational mobility. Therefore, they require the surplus
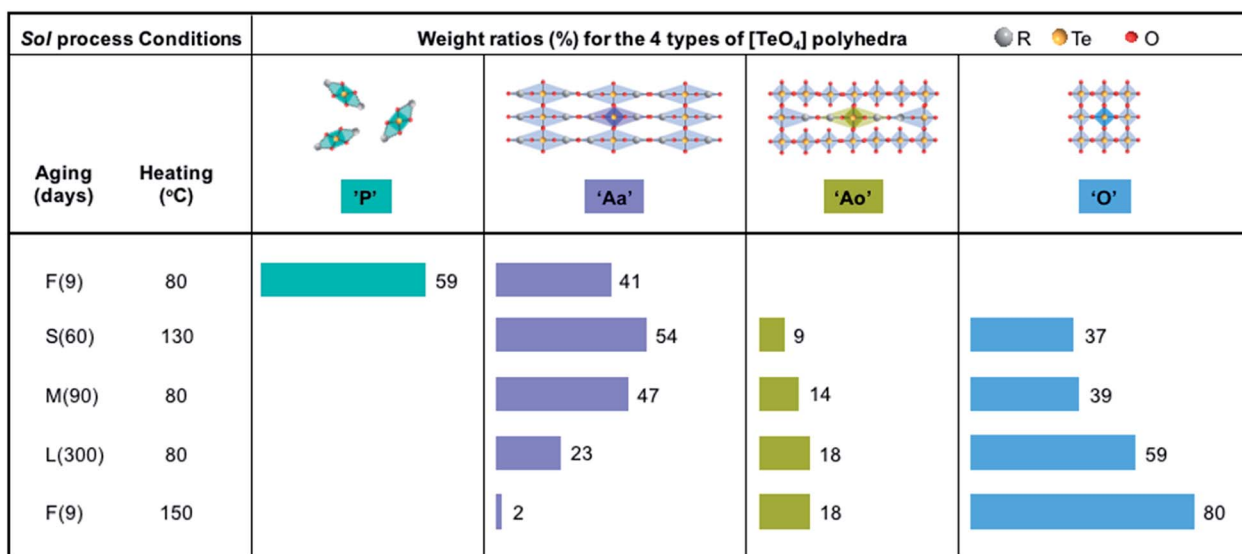

Sol process Conditions		Weight ratios (%) for the 4 types of $[TeO_4]$ polyhedra			
Aging (days)	Heating (°C)	'P'	'Aa'	'Ao'	'O'
F(9)	80	59	41		
S(60)	130		54	9	37
M(90)	80		47	14	39
L(300)	80		23	18	59
F(9)	150		2	18	80

Fig. 6 Schematic illustration of the 4 types of $[TeO_4]$ polyhedra constituting the xerogel network: 'P' polyhedron: ; 'Aa' polyhedron: ; 'Ao' polyhedron: ; and 'O' polyhedron: . The deep-color squared frames of the molecular structures designate the $[TeO_4]$ polyhedron, and the light-color regions specify the atoms belonging to a $[TeO_4]$ polyhedron in terms of respective weight ratio. The horizontal colored bars designate the weight ratios of the different types of polyhedra in the xerogels prepared using different times and temperatures.
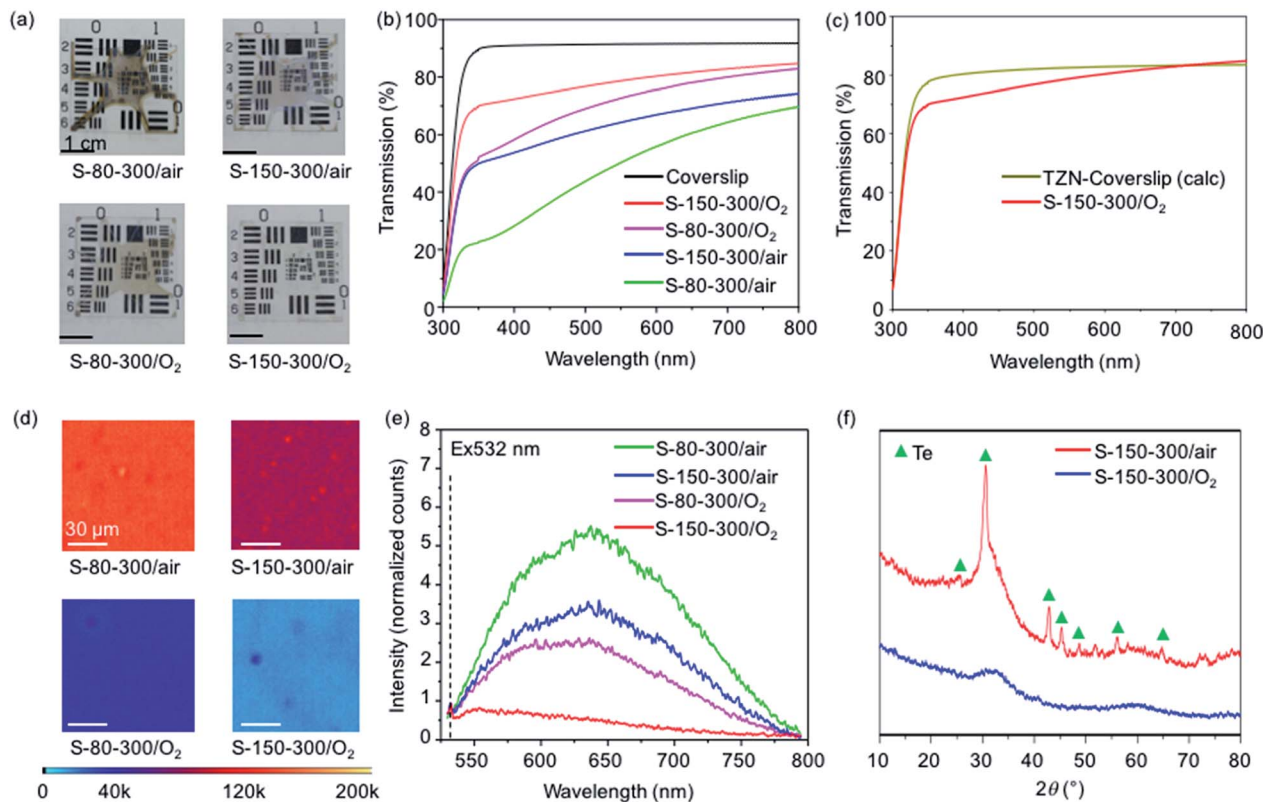
Fig. 7 Optical and structural characterizations of TZN glass films prepared under different temperatures and atmospheres in the course of sol heating and xerogel heating. (a) Photographs and (b) experimental transmission spectra of various xerogel samples. (c) Theoretical transmission spectrum of $75TeO_2-15ZnO-10Na_2O$ glass[20] on D 263™ T coverslip, relative to the measured transmission spectrum of S-150-300/O_2. (d) Confocal microscope images, and (e) fluorescence spectra of TZN glass films on glass coverslips. The fluorescence spectra were taken from arbitrary spots of the films and normalized to the excitation power of 532 nm (2.56 µW for all measurements). (f) Micro-XRD patterns of TZN films on Si wafers, showing the characteristic diffractions of metallic–Te and the amorphous structure with a broad 'hump' at ~32°.

energy of exothermic combustion to liberate OGs, leading to weight loss in the high temperature range region III.

• 'O' polyhedra do not have alkoxy bridges and thus do not show OG liberation. They constitute the weight remains at the end temperature of region III.

3.3.4. Interrelation of sol aging time and heating temperature on OGs content in xerogel samples. The characteristic thermal behavior of each type of $[TeO_4]$ polyhedron allows us to determine their weight fractions in the respective xerogel samples (detailed explanation and calculation given in the ESI associated with Fig. S6†).

The F-80 xerogel consists of 'Aa' polyhedra (41 wt%) and 'P' polyhedra (59 wt%). The large portion of 'P' polyhedra suggests that only a portion of the precursor molecules is involved in polymerization due to the short sol aging time (e.g., 9 days) and the low sol heating temperature (e.g., 80 °C over 3 days). The absence of 'Ao' and 'O' polyhedra indicates that the condensation reaction does not proceed to a considerable extent during the short sol aging time and at the low sol heating temperature. The evaporation of 'P' polyhedra during heating of F-80 xerogel causes large weight loss (Te-alkoxide precursor begins to evaporate at 100 °C, Fig. S7†), suggesting the F-80 xerogel is not an appropriate option to prepare a glass film.

For the M-80 and L-80 xerogel samples, the fractions of 'Ao' and 'O' polyhedra increases with sol aging time. This indicates that condensation reaction occurs progressively as a function of sol aging time, which consequently increases the fractions of 'Ao' and 'O' polyhedra, leading to a reduced amount of OGs that is liberated during xerogel heating.

Compared to S-130, M-80 contains a lower amount of 'Aa' polyhedra but higher amounts of 'Ao' and 'O' polyhedra (Fig. 6). Since the condensation reaction is facilitated with prolonged aging time, this result indicates that the longer sol aging time (90 days for M-80 versus 60 days for S-130) considerably increases the formation of 'Ao' and 'O' polyhedra.

Despite the short aging time of only 9 days, F-150 shows a network mainly composed of 'O' and 'Ao' polyhedra with minor portions of 'Aa' polyhedra (Fig. 6). This result indicates that, due to thermally enhanced bond cleavage and re-arrangement, 150 °C sol heating temperature particularly facilitates the condensation reaction.

The different portions of $[TeO_4]$ polyhedra in F-80 and F-150 xerogel samples account for their different behavior in the liberation of OGs. Due to the evaporation of 'P' polyhedra and decomposition of 'Aa' polyhedra F-80 shows only a DTG peak in region II, while due to combustion of 'Ao' polyhedra, F-150 presents almost only a DTG peak in region III. To shed more

light on the liberation of OGs *via* decomposition and combustion in different temperature regions, these two samples with contrasting thermal behavior were analyzed by vapor-FTIR spectroscopy.

Fig. S8† displays the temperature dependence of the FTIR bands for the vibrational bonds O–H (stretching: 3400 to 3700 cm^{-1}), C=O (stretching: 1700 to 1830 cm^{-1}),[51,52] C–H (stretching: 2800 to 2931 cm^{-1}, bending: 1300 to 1400 cm^{-1}),[53,54] C–O (stretching: 917 to 1226 cm^{-1}),[55] and Te–O (stretching: 600 to 660 cm^{-1} in [TeO$_4$] polyhedron).[56] The F-80 sample shows released compounds with Te–O and C–H bonds as well as an increased amount of compounds with C–O and C=O bonds in the range of 180–210 °C. This agrees with the TG-DSC results, showing precursor evaporation and alkoxy bridge decomposition starting at >100 °C, peaking at 219 °C and finishing at 230 °C. No enhanced amount of CO$_2$ was found in the gaseous release from the F-80 sample. By contrast, the F-150 sample shows no C–H, C–O and C=O groups but release of vapor containing CO$_2$ which appears at 220 °C and reaches highest amount at 300 °C. The release of CO$_2$ due to combustion is in good agreement with the TG-DSC result of F-150 sample, which shows combustion commencing at 250 °C, peaking at 269 °C and finishing at 300 °C. The absence of Te–O bonds in the vapor-FTIR of F-150 sample indicates a lack of precursor evaporation, which is consistent with the TG-DSC result and ascribed to the high degree of polymerization.

It is also worth noting that with increasing 'Ao' and 'O' polyhedra content, the peak temperature of the decomposition increases while the peak temperature for combustion slightly decreases (Fig. S9†). The increased 'Ao' and 'O' contents are accompanied with enhanced steric hindrance and reduced amount of OGs. A higher steric hindrance hampers the decomposition, thus requiring higher thermal activation. The lower amount of OGs is likely to facilitate the combustion, leading to reduced combustion temperature. These results consolidate the correlation of the decomposition and combustion with the steric hindrance imposed by oxo bridges around alkoxy bridges.

In summary, the high sol heating temperature of 150 °C was found to have a remarkable impact. Compared to both S-130 and L-80, F-150 has a higher amount of 'O' polyhedra despite the short sol aging time of 9 days relative to 30 days for S-130 and even 300 days for L-80. This indicates that the effect of temperature increase from 80 or 130 to 150 °C counterbalances the effect of sol aging time decrease from 300 or 30 to 9 days. The highest amount of 'O' polyhedra for F-150 of all xerogel samples suggests that its xerogel network is mainly formed *via* condensation. As a result, a large amount of OGs is liberated during xerogel preparation and only a small residual amount of OGs is released during xerogel heating. This is beneficial to suppress the formation of metallic-Te.

3.3.5. Suppressing metallic-Te formation by the provision of O$_2$. For the xerogel samples heated under dry air, the endothermic DSC peak at ~449 °C corresponds to the melting of metallic-Te. This suggests that even the lowest amount of OGs in the F-150 xerogel causes the formation of metallic-Te when heated in air. Therefore, in order to suppress the metallic-Te

formation, the liberated OGs need to be oxidized prior to their involvement in reducing Te(IV). For this purpose, the impact of O$_2$ during xerogel heating was investigated *via* TG-DSC measurement of the S-130 xerogel sample (containing a medium amount of OGs of all investigated xerogel samples). This TG-DSC analysis was carried out under O$_2$-rich atmosphere (80% O$_2$ and 20% N$_2$) compared to dry air (20% O$_2$ and 80% N$_2$). The purging of O$_2$-rich atmosphere during xerogel heating eliminated the melting peak of metallic-Te (449 °C) (Fig. 4e *versus* 4f), which proves that the provision of O$_2$ facilitates the oxidization of the liberated OGs and thus has the potential to prevent metallic-Te formation.

3.4. Optimal chemical route to synthesize metallic-Te free TZN glass film

The insights into formation, evolution and thermal behavior of different types of [TeO$_4$] polyhedra in xerogel samples demonstrated that the appropriate choice of sol aging time, sol heating temperature, and O$_2$ atmosphere is critical. To identify the optimal synthesis conditions for transparent TZN glass films, conditions that enable complete transformation of precursor molecules into a xerogel network and finally a dense OG-free and crystal-free glass structure were selected. Specifically, short sol aging time (20–80 days), low and high sol heating temperatures (80 °C and 150 °C), and xerogel heating temperature (300 °C) were investigated (S-80-300 and S-150-300 samples). In addition, impact of dry O$_2$ flow compared to ambient air atmosphere was explored. It is worthwhile to note that dry O$_2$ flow was used during both the sol heating and the xerogel heating processes. O$_2$ flow during sol heating allows diffusion of excess O$_2$ into the xerogel films, which is then available to react with the liberated OGs in the subsequent xerogel heating process. O$_2$ flow during xerogel heating is conducted to suppress the out-diffusion of O$_2$ from xerogel films.

To quantitatively analyze the content of metallic-Te in the glass films, optical micrograph, UV-Vis transmission spectroscopy, confocal microscopy and fluorescence spectroscopy were utilized.

For both air and O$_2$ atmosphere, the S-150-300 samples exhibit lower intensities of the characteristic metallic-Te properties (brown color, reduced UV-Vis transmission and presence of fluorescence) than the S-80-300 samples (Fig. 7). The higher sol heating temperature of S-150-300 enhances the condensation reaction, which decreases the amount of OGs and thus suppresses the metallic-Te formation.

For the glass films prepared at the same sol heating temperature, the use of O$_2$ flow markedly reduces the intensities of the characteristic metallic-Te properties (Fig. 7). However, for the S-80-300/O$_2$ sample, light brown color, and slightly reduced UV-Vis transmission and pronounced fluorescence were still observed. This indicates that inhibiting the metallic-Te formation cannot only rely on the use of O$_2$, but must be used in combination with suitable sol aging time and sol heating temperature.

The S-150-300/O$_2$ film shows the absence of the characteristic metallic-Te properties, as well as the omission of the characteristic diffractions of metallic-Te. As a result, the S-150-

300/O_2 film shows a transmission that is closest to the theoretical transmission limit given by the Fresnel reflection for a TZN film on a coverslip and the UV edge of the coverslip (Fig. 7c, calculation of the theoretical transmission limit provided in ESI†).[20] Specifically, the transmission is within 10% of the theoretical limit for wavelengths <700 nm and at the theoretical limit for wavelengths >700 nm. The lower transmission between 350–700 nm is attributed to the Rayleigh scattering effect of the film surface roughness.

4.   Conclusions

We have elucidated the mechanisms of forming metallic-Te during the different steps of the NHSG route. We unraveled that the use of O_2 during the film preparation is not sufficient to completely prevent the metallic-Te formation, since the amount of OGs in the xerogel films plays a decisive role in determining the formation of metallic-Te during the subsequent heating to form a dense glass film. Therefore, the use of O_2 need to be combined with appropriate choice of sol aging time and sol heating temperature to minimize the amount of OGs in the xerogel films.

This in-depth understanding allowed us to develop a synthesis protocol to produce metallic-Te free TZN films. Firstly, we applied sol aging at room temperature for 30–60 days, which allowed all precursor molecules to undergo polymerization *via* addition and condensation reactions. Secondly, we used sol heating temperature at 150 °C to accelerate the condensation reaction, which leads to the highest 'O' polyhedra content and the lowest OGs fractions of all xerogel samples investigated. Thirdly, we constantly purged O_2 during both the sol heating at 150 °C and the xerogel heating at 300 °C, so that the liberated OGs react with the O_2 to form volatile gases rather than with Te(ɪv) to generate metallic-Te.

The absence of metallic-Te in the TZN film synthesized using these optimal conditions led to a high optical transmission over the whole intrinsic transmission window of tellurite glass, *i.e.* from the UV to the infrared range. To the best of our knowledge, this is the highest transmission achieved for a tellurite sol–gel glass films relative to the theoretical limit. Reducing the surface roughness of the films is expected to minimize the scattering-induced transmission loss in the visible spectral range. The preparation of high-transmission TeO_2-based sol–gel glass films paves the way to develop hybrid optoelectronic films by incorporating diverse nanoparticles with unique functionalities.

Funding sources

Conflicts of interest

There are no conflicts to declare.

Abbreviations

NPs	Nanoparticles
TZN	TeO_2–ZnO–Na_2O
NHSG	Non-hydrolytic sol–gel
OGs	Organic groups
R	$CH(CH_3)$–CH_2
F	Fresh-aged
S	Short-aged
M	Medium-aged
L	Long-aged
LPE	Lone pair electrons

Acknowledgements

References

1 Y. Wei, H. Ebendorff-Heidepriem and J. Zhao, *Adv. Opt. Mater.*, 2019, 1900702.

2 A. Llordés, G. Garcia, J. Gazquez and D. J. Milliron, *Nature*, 2013, **500**, 323–326.

3 M. Li, S. Magdassi, Y. Gao and Y. Long, *Small*, 2017, **13**, 1701147.

4 J.-S. Kim, S. C. Yang, S.-Y. Kwak, Y. Choi, K.-W. Paik and B.-S. Bae, *J. Mater. Chem.*, 2012, **22**, 7954–7960.

5 P.-T. Chung, S.-H. Chiou, C.-Y. Tseng and A. S.-T. Chiang, *ACS Appl. Mater. Interfaces*, 2016, **8**, 9986–9993.

6 J. Lee, Y. Y. Kwon, E.-H. Choi, J. Park, H. Yoon and H. Kim, *Opt. Express*, 2014, **22**, A705–A714.

7 S. Brovelli, N. Chiodini, R. Lorenzi, A. Lauria, M. Romagnoli and A. Paleari, *Nat. Commun.*, 2012, **3**, 690.

8 C. W. Hsu, B. Zhen, W. Qiu, O. Shapira, B. G. DeLacy, J. D. Joannopoulos and M. Soljačić, *Nat. Commun.*, 2014, **5**, 3152.

9 Y. Ohko, T. Tatsuma, T. Fujii, K. Naoi, C. Niwa, Y. Kubota and A. Fujishima, *Nat. Mater.*, 2003, **2**, 29.

10 X. Luo, T. Ding, X. Liu, Y. Liu and K. Wu, *Nano Lett.*, 2018, **19**, 338–341.

11 S. Reda, *Acta Mater.*, 2008, **56**, 259–264.

12 Z. Fang, Y. Li, F. Zhang, Z. Ma, G. Dong and J. Qiu, *J. Am. Ceram. Soc.*, 2015, **98**, 1105–1110.

13 S. T. Selvan, C. Bullen, M. Ashokkumar and P. Mulvaney, *Adv. Mater.*, 2001, **13**, 985–988.

14 L. Korala, Z. Wang, Y. Liu, S. Maldonado and S. L. Brock, *ACS Nano*, 2013, **7**, 1215–1223.

15 J. W. Chon, C. Bullen, P. Zijlstra and M. Gu, *Adv. Funct. Mater.*, 2007, **17**, 875–880.

16 X. Yan, F. W. Mont, D. J. Poxson, M. F. Schubert, J. K. Kim, J. Cho and E. F. Schubert, *Jpn. J. Appl. Phys.*, 2009, **48**, 120203.

17 Z. Remes, A. Kromka, M. Vanecek, A. Grinevich, H. Hartmannova and S. Kmoch, *Diamond Relat. Mater.*, 2007, **16**, 671–674.

18 B. Davis and D. Keller, *Appl. Phys. Lett.*, 1964, **5**, 80–81.

19 N. Hondow, R. Brydson, P. Wang, M. D. Holton, M. R. Brown, P. Rees, H. D. Summers and A. Brown, *J. Nanopart. Res.*, 2012, **14**, 977.

20 J. Zhao, X. Zheng, E. P. Schartner, P. Ionescu, R. Zhang, T. L. Nguyen, D. Jin and H. Ebendorff-Heidepriem, *Adv. Opt. Mater.*, 2016, **4**, 1507–1517.

21 B. O'regan and M. Grätzel, *nature*, 1991, **353**, 737.

22 R. Boidin, T. Halenkovič, V. Nazabal, L. Beneš and P. Němec, *Ceram. Int.*, 2016, **42**, 1177–1182.

23 T. Siefke, S. Kroker, K. Pfeiffer, O. Puffky, K. Dietrich, D. Franta, I. Ohlídal, A. Szeghalmi, E. B. Kley and A. Tünnermann, *Adv. Opt. Mater.*, 2016, **4**, 1780–1786.

24 D. L. Wood and K. Nassau, *Appl. Opt.*, 1982, **21**, 2978–2981.

25 B. Hu, M. Yao, R. Xiao, J. Chen and X. Yao, *Ceram. Int.*, 2014, **40**, 14133–14139.

26 Z. Su, M. Yao, M. Li, W. Gao, Q. Li, Q. Feng and X. Yao, *J. Mater. Chem. C*, 2018, **6**, 5616–5623.

27 S. Seidel, A. Sabelfeld, R. Strohmeyer, G. Schreiber, V. Klemm, D. Rafaja, Y. Joseph and J. Heitmann, *Thin Solid Films*, 2016, **606**, 13–18.

28 N. Uchida, *Phys. Rev. B: Solid State*, 1971, **4**, 3736.

29 B. Zheng, M. Zhao, Q. Guo, Y. Yu, S. Lu, X. Jiang and S. Zhou, *J. Mater. Chem. C*, 2015, **3**, 5141–5144.

30 H.-y. Wei, J. Lin, W.-h. Huang, Z.-b. Feng and D.-w. Li, *Mater. Sci. Eng., B*, 2009, **164**, 51–59.

31 S. Hodgson and L. Weng, *J. Non-Cryst. Solids*, 2000, **276**, 195–200.

32 A. Lecomte, F. Bamiere, S. Coste, P. Thomas and J.-C. Champarnaud-Mesjard, *J. Eur. Ceram. Soc.*, 2007, **27**, 1151–1158.

33 C. J. Brinker and G. W. Scherer, *Sol-gel science: the physics and chemistry of sol-gel processing*, Academic press, 2013.

34 S. Hodgson and L. Weng, *J. Sol-Gel Sci. Technol.*, 2000, **18**, 145–158.

35 T. Hayakawa, H. Koyama, M. Nogami and P. Thomas, *J. Univ. Chem. Technol. Metall.*, 2012, **47**, 381–386 .

36 S. Hodgson and L. Weng, *J. Mater. Sci.: Mater. Electron.*, 2006, **17**, 723–733.

37 L. Weng, S. Hodgson, X. Bao and K. Sagoe-Crentsil, *Mater. Sci. Eng., B*, 2004, **107**, 89–93.

38 L. Weng, S. Hodgson and J. Ma, *J. Mater. Sci. Lett.*, 1999, **18**, 2037–2039.

39 M. P. Mahindaratne and K. Wimalasena, *J. Org. Chem.*, 1998, **63**, 2858–2866.

40 Z. Zhang, C. Xie, L. Feng and C. Ma, *Synth. Commun.*, 2016, **46**, 1507–1518.

41 S. A. Girard, H. Huang, F. Zhou, G.-J. Deng and C.-J. Li, *Org. Chem. Front.*, 2015, **2**, 279–287.

42 O. Ogbuu, Q. Du, H. Lin, L. Li, Y. Zou, E. Koontz, C. Smith, S. Danto, K. Richardson, J. Hu and P. Lucas, *J. Am. Ceram. Soc.*, 2015, **98**, 1731–1738.

43 M. Henderson, B. Gibson, H. Ebendorff-Heidepriem, K. Kuan, S. Afshar V, J. Orwa, I. Aharonovich, S. Tomljenovic-Hanic, A. Greentree and S. Prawer, *Adv. Mater.*, 2011, **23**, 2806–2810.

44 O. Lindqvist, *Acta Chem. Scand.*, 1967, **21**, 1473–1483.

45 Y. Cheng, N. Yan, X. Han, Z. Zhang, T. Zhang, Z. Song, B. Liu and S. Feng, *J. Non-Cryst. Solids*, 2010, **356**, 884–888.

46 A. Nukui, T. Taniguchi and M. Miyata, *J. Non-Cryst. Solids*, 2001, **293**, 255–260.

47 D. W. Lee and K. M. Ok, *Inorg. Chem.*, 2014, **53**, 10642–10648.

48 A. Šantić, A. Moguš-Milanković, K. Furić, M. Rajić-Linarić, C. S. Ray and D. E. Day, *Croat. Chem. Acta*, 2008, **81**, 559–567.

49 A. Vioux, *Chem. Mater.*, 1997, **9**, 2292–2299.

50 W. Vogel, *Glass chemistry*, Springer Science & Business Media, 2012.

51 C. Y. Tang, Y.-N. Kwon and J. O. Leckie, *Desalination*, 2009, **242**, 149–167.

52 H. Yang, R. Yan, H. Chen, D. H. Lee and C. Zheng, *Fuel*, 2007, **86**, 1781–1788.

53 C. P. Marshall, E. A. Carter, S. Leuko and E. J. Javaux, *Vib. Spectrosc.*, 2006, **41**, 182–189.

54 F. Carrillo, X. Colom, J. Sunol and J. Saurina, *Eur. Polym. J.*, 2004, **40**, 2229–2234.

55 B. H. Liu, L. T. Dou, F. He, J. Yang and Z. P. Li, *RSC Adv.*, 2016, **6**, 19025–19033.

56 M. Çelikbilek, A. Erçin Ersundu and S. Aydin, *J. Am. Ceram. Soc.*, 2013, **96**, 1470–1476.